

Process Mapping of Inconel 625 in Laser Powder Bed Additive Manufacturing

Colt Montgomery^a, Jack Beuth^a, Luke Sheridan^b, Nathan Klingbeil^b

^aCarnegie Mellon University, ^bWright State University

Abstract

Understanding laser powder bed additive manufacturing of nickel superalloys is important for the widespread adoption of the technology. To promote adoption, melt pool geometry as well as microstructure prediction and control must be thoroughly understood. In this research Inconel 625 is investigated to determine optimal regions of processing space within the laser powder bed operating range. Single bead and pad geometries are investigated along with solidification microstructure and defects by utilizing a process mapping approach. The effect of powder addition on the process is also examined. Results from models are compared with experimental results to verify modeling techniques. Insights are gathered by comparing these results to those of other alloy systems in the laser powder bed operating space.

Introduction

Additive Manufacturing (AM) has the potential to revolutionize manufacturing but before the technology can replace traditional methods there must be a thorough understanding process outcomes such as melt pool geometry, solidification microstructure, and residual stress [1] [2] [3]. Currently there is a lack of understanding as to how to relate processing variables between alloy systems and across different metal AM technologies and processes. Even within a given technology there is limited knowledge as to the effects of altering the process variables (power, velocity, preheat temperature, etc.) outside of standard manufacturer established process variable sets for a given alloy [4].

Inconel Alloy 625 (IN625) is an engineered Nickel-Chrome superalloy with high strength, high corrosion resistance, and excellent fatigue resistance [5]. For these reasons IN625 is an excellent candidate for marine and nuclear applications where corrosion is of major concern. IN625 maintains these properties over a wide range of temperatures which makes it suitable for aerospace applications and chemical plants [5]. Conventional machining of IN625 is difficult because of excessive wear on the tooling and slow material removal rates. These factors make it an ideal candidate for AM technologies [6] [7]

Background

Gockel [1] was able to predict the microstructure in Ti-6Al-4V deposits by controlling the process variables for Electron Beam Melting (EBM) and Wire-Feed e-beam systems. Experimental characterization of IN625 microstructure in EOS-built parts is being pursued at the University of Louisville [6]. While the effect of process variables on mechanical properties of various alloys produced by Selective Laser Melting (SLM) have been studied by various groups [8] [6] [9] [10]; melt pool geometry control has not been researched for the SLM process in great detail. Melt pool geometry control is important to AM because it allows end users to efficiently and effectively produce parts with desired characteristics such as geometric precision [11].

The goals of this research are to transfer process mapping techniques previously developed for other AM technologies and alloy systems to the EOS laser powder bed process for IN625, estimate the laser absorptivity, as well as determine the effect of powder on melt pool geometry and microstructure.

Methods

Process Mapping:

Process mapping is an approach developed by Beuth et al. [3] to simply illustrate the process outcomes of an AM process based on process input parameters. These parameters are often conveniently displayed as two independent variables, power and velocity, while the other variables such as preheat temperature, feed rate (or layer thickness), and feature geometry remain fixed [3], with the resulting outcome of these parameters shown on the resulting 2-D plot. An example of the different regions of power and velocity (P-V) space can be seen in Figure 1. Commonly plotted are curves of constant cross sectional area (Figure 2) which show what power and velocity combinations will result in a similar melt pool cross sectional areas. Currently the authors have ongoing work in all of the direct metal additive manufacturing processes and in a variety of alloy systems looking at several different process outcomes.

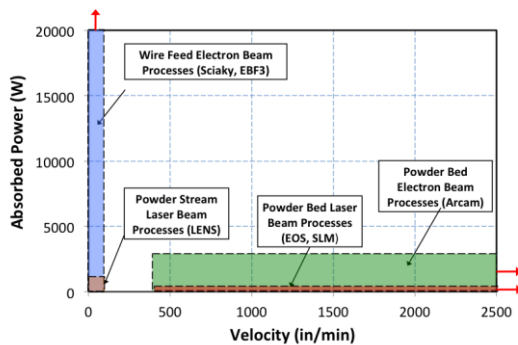


Figure 1: P-V Map of different operating regions

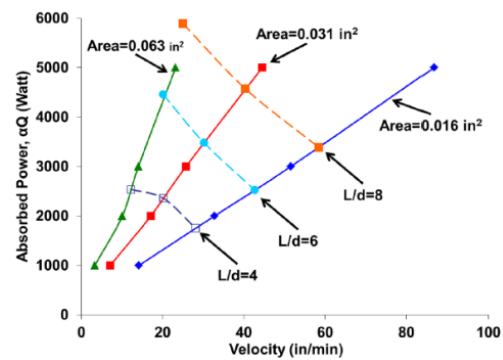


Figure 2: Example P-V map of curves of constant cross sectional area

Experiments:

Experiments were performed by the National Institute of Standards and Technology (NIST) using an EOSINT M270 Laser Powder Bed system on an IN625 plate. A test matrix of various power and velocity combinations was created, which can be seen graphically in Figure 3. The combinations were selected to span the entire standard operating region of the EOSINT M270 machine. The single bead tests were laid out as shown in Figure 4, with fourteen groups of settings, along with a single pad at nominal settings, for future work, on each plate. Each group represents a single bead run at a constant power with each square path run at a different velocity at that power. Two groups of tests per power were performed, resulting in six different velocities for each of the seven powers, totaling 42 different combinations. These tests were done on two plates, one without any added powder, and one with a 20 μm layer of powder added.

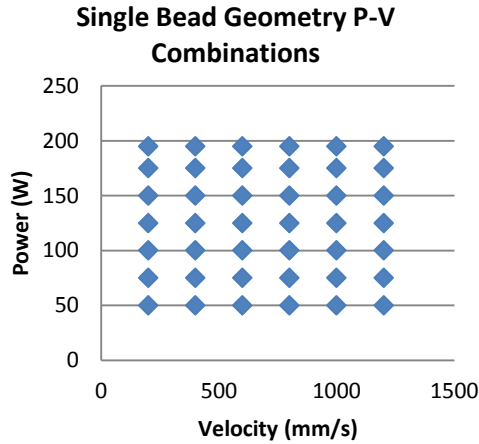


Figure 3: Power and velocity combinations tested for single bead geometry

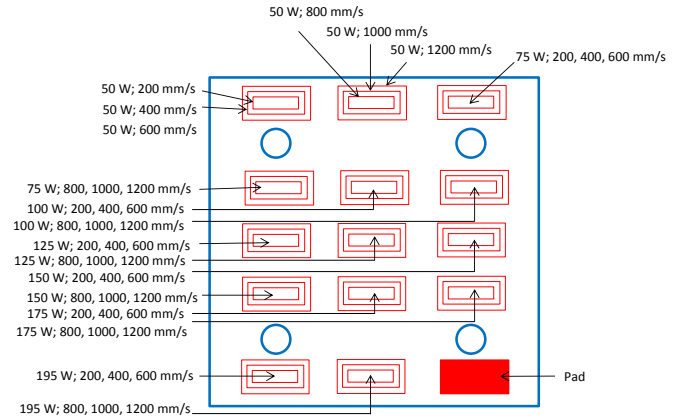


Figure 4: Single bead geometry test layout

Single layer and multi-layer pad experiments were then performed to analyze the differences in pad geometries compared to the single bead geometry. Again, a test matrix (Figure 5) of various power and velocity combinations was created that spanned the entire EOS standard operating region. Twenty-four different pads were created per plate and the experimental layout along with exposure order can be seen in Figure 6. The tests were done on three plates, one without any added powder, another with a single 20 μm layer of powder, and finally a pad built with ten 20 μm layers of material. Each pad utilizes a scaled hatch spacing to attempt to maintain the nominal overlap (approximately 24%) between melt pools. The scaled hatch spacing was calculated from single bead widths and the overlap produced using the EOS default parameters for pads.

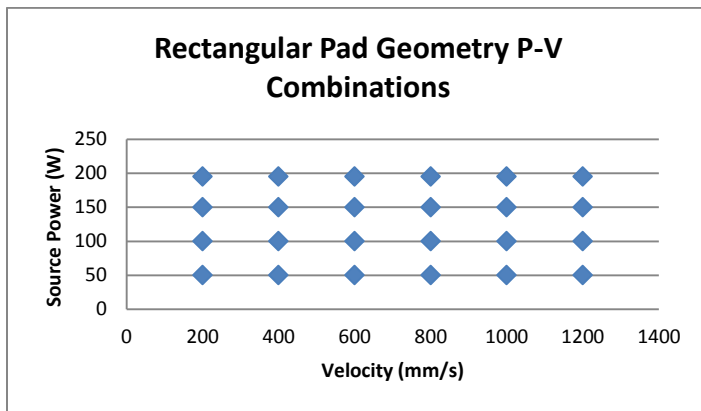


Figure 5: Power and Velocity combinations tested for pad geometries

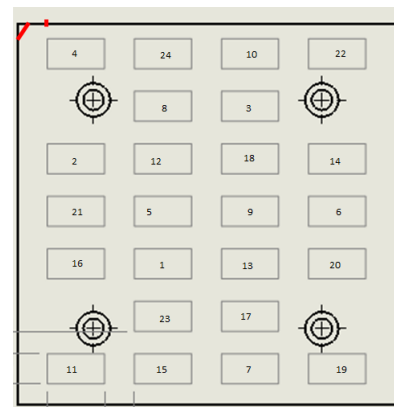


Figure 6: Pad geometry test layout and exposure order

No Powder Finite Element Model:

A numerical 3-D finite element model was created to simulate the laser powder process. The model is similar to the model created by Soylemez [11], but without the addition of material. The model is initialized at 80°C and maintains a constant base temperature of 80°C to simulate the preheating during the actual process. All other surfaces are insulated by the default boundary condition. The current model does not include convection or radiation because conduction is the

primary heat transfer mechanism in the process. The model includes latent heat effects and contains temperature-dependent material properties of IN625 including density, specific heat, and thermal conductivity.

The model is constructed so that the free edges are sufficiently far enough away as to have no effect on the melt pool, simulating the large base plate that the deposition occurs on. A symmetric boundary condition is imposed on the mid-plane to reduce computation time. A distributed heat flux is applied along the top of the model simulating the application of the laser to the material to induce melting. The applied flux travels along the axis of symmetry to simulate the movement of the beam. An example of the model can be seen in Figure 7. The melt pool cross sectional area is defined as the largest steady state cross sectional area in the plane perpendicular to the travel direction of the beam that reaches melting temperature. The melt pool width is the maximum steady state width of the melt pool at the surface.

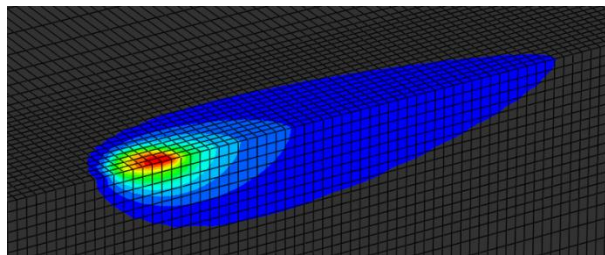


Figure 7: Finite element model example melt pool

Powder Finite Element Model:

A novel finite element model simulating the thermal effects of added powder has been developed. The model utilizes the basic model structure used previously by the group but adds a layer of powder to the top. The model aims to simulate the macro-scale effects of the powder on the thermal problem and melted geometry, not to simulate induced porosity or other effects known to occur as the result of powder variation [2].

There was difficulty in changing the volume of the elements in the FEA model so a constant volume and density (to maintain conservation of mass) approach was utilized. To account for the changes in density that are not being directly simulated, the conductivity is scaled appropriately. Specific heat is maintained as constant because this is tied to density in the heat transfer equations and changing this value would violate the conservation of energy. The model changes the material properties from those of powder to those of a fully dense material once the solidus temperature is reached. For the results that follow a packing factor of 0.5 is assumed as a conservative estimate, so a 20 μm layer will appear as a 10 μm layer in the model but have thermal properties consistent with the 20 μm layer. The thermal properties of the powder are assumed to be a fraction of those of the fully dense material keeping in mind that contact resistance will decrease the thermal conductivity substantially. Currently the model only incorporates a linear scaling of properties until the solidus temperature is reached, this can be readily adapted to account for different thermal models.

Results

A process map was constructed for curves of constant area based on the experimental results from the single bead tests and can be seen in Figure 8 along with examples of where

keyholing is observed to occur and examples of a keyholed melt pool and a standard melt pool. The colors represent a given cross sectional area while the triangles represent no added material results and the squares represent 20 μm added material results. The curves look similar to what the author's group has published in the past for other alloys [12] [4] [11]. The powder and no powder results appear to be nearly indistinguishable from each other for most of P-V space, which provides evidence that the role of the powder could be neglected in certain regions of P-V space for certain layer thicknesses. It is predicted that keyholing will occur in regions of high power and low velocity based on these images and previous (and ongoing) work by the authors in other alloy systems.

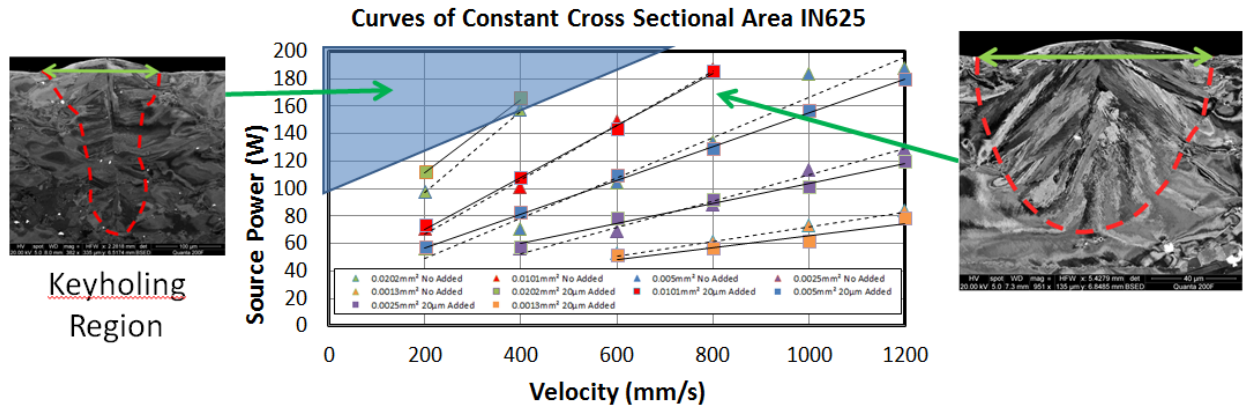


Figure 8: Experimental curves of constant cross sectional area for IN625 and an annotation for the keyholing region. Colors represent a given cross sectional area

A simulation-based process map in P-V space was also constructed for IN625. The simulation results are in terms of absorbed power, so a scaling factor must be applied to compare them with the experimental results. The effective absorptivity is a factor that can be used to account for the true absorptivity of laser power, as well as the minor effects not included in the models, such as convection, radiation, and powder effects. The average effective absorptivity factors for IN625 powder and no powder in the EOS process were calculated to be approximately 0.57 which is similar to the literature value for Inconel of up to 0.52 for a Nd:YAG laser of similar wavelength to the Yb:YAG laser used in the EOS machine [13] [14]. By applying the absorptivity to the experimental results, the absorbed power to achieve a desired melt pool area can be found. These scaled experimental results overlaid on top of the simulation-derived cross sectional areas can be seen in Figure 9. These results correspond reasonably well but not perfectly and a varying absorptivity would likely correlate better.

From these results we can see a possible dependence on cross sectional area for absorptivity. A larger melt pool appears to absorb more power than a smaller one. This is in contrast to results for curves of constant width, which suggest less variance in the absorptivity and have a best-fit absorptivity of approximately 0.51 over the span of P-V space being investigated. Currently the cross sectional area dependence is believed to possibly be because of a higher absorptivity with higher surface temperatures, which would be seen under the beam for large melt pool sizes (and a fixed beam focus).

IN625 Single Bead Experiments Vs. Simulations Curves of Constant Cross Sectional Area

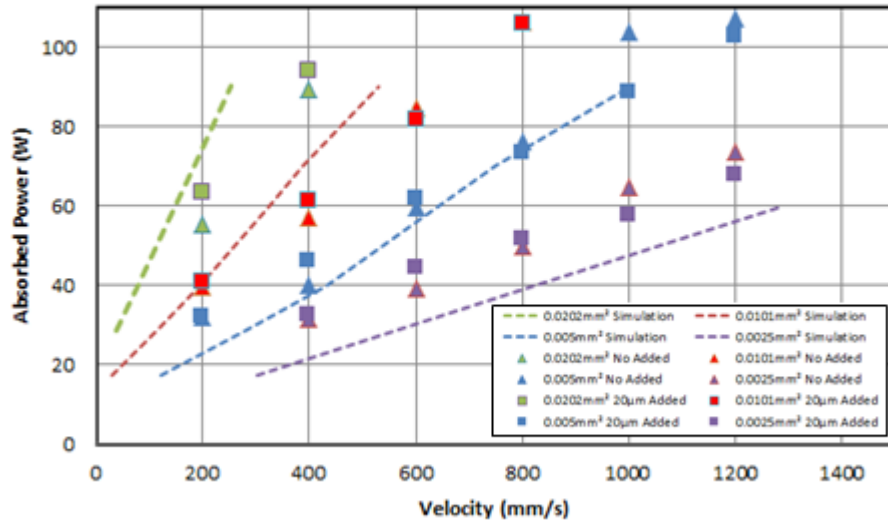


Figure 9: Comparison of experimental and simulation curves of constant cross sectional area

Single Layer Pads

Figure 10 shows a single bead P-V combination compared to the pad geometry of the same P-V in Figure 11. It is readily apparent that keyholing is evident in both cases (as predicted) and that the resulting melt pools are of similar depth. This ability to predict melt pool effects based on single bead experimentation is beneficial since running single bead experiments and analysis can be done faster than running pad experiments.

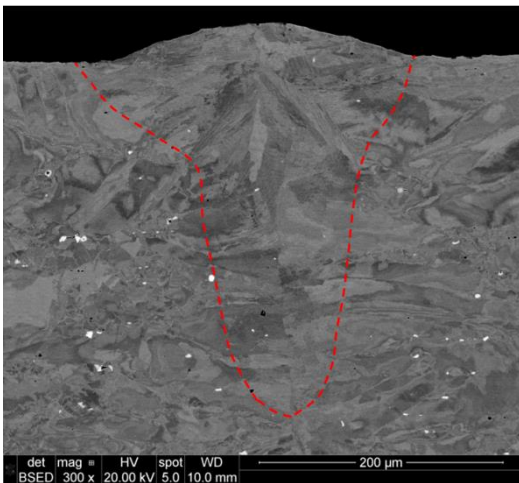


Figure 10: Keyholing in single bead geometry

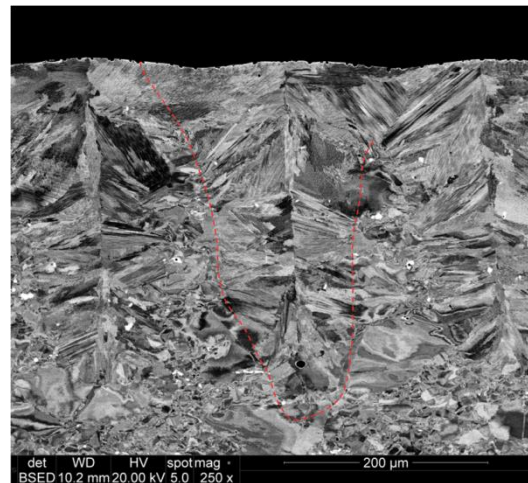


Figure 11: Keyholing in single layer of powder pad

Comparing single layer pads of no powder added to those with 20 µm of added material it becomes readily apparent that the powder changes the geometry of the melted region very little. The images in Figure 12 and Figure 13 show the same melt pool but for both no powder and powder respectively. It can be seen that the overlap appears to be what was expected

(approximately 24%) and that the microstructure appears to be similar between the two. This implies that the 20 μm of powder does not change the thermal problem very much.

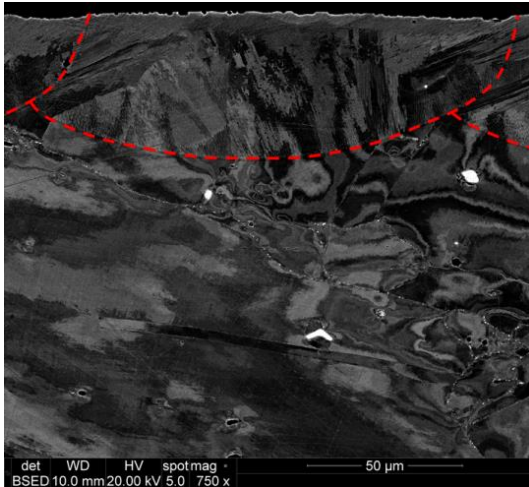


Figure 12: No added material pad

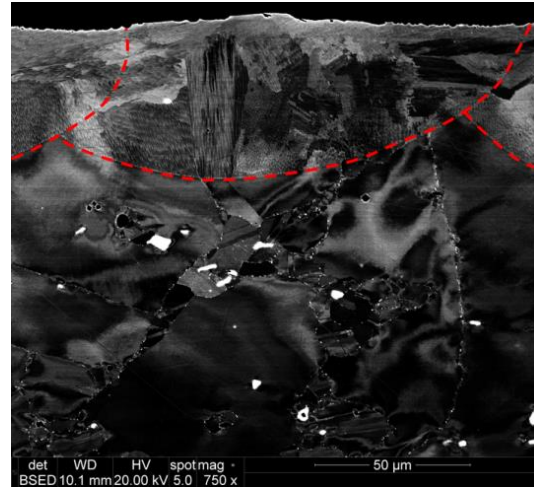


Figure 13: Single layer 20 μm of powder pad

Preliminary Microstructural Observations in Multi-Layer Pads

Microstructure is clearly evident in the experimental results but to get a more accurate microstructural analysis EBSD will be performed in future work. Preliminary observations show that grains appear to be epitaxial and growing through the middle of the melt pool. The grains can be seen to be growing through multiple layers as well in Figure 14.

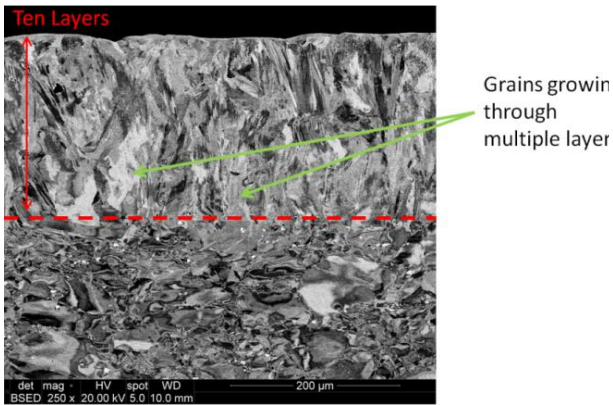


Figure 14: Grains growing through multiple layers

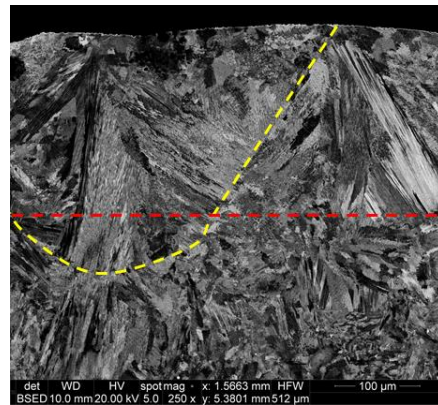


Figure 15: Large melt pool in multiple layer tests where the melt pool is outlined in yellow and the powder layers are above the red dashed line

In general in the multilayer pads' melt pools are not clearly visible because the melt pools are obliterated as other layers are deposited on top of previous layers. Multilayer pad microstructure appears to be larger than what was observed in the single bead and single layers tests. This is likely because of the increase in time that the part stays at an elevated temperature as the build progresses. It can also be seen in Figure 15, where the melt pool is outlined in yellow and the powder layers are above the red dashed line, that when melt pools are exceptionally large they are still visible after 10 layers but this is believed to be because of the melt pool being larger than the combined melted layers. The depth in Figure 15 agrees with single bead results. Although

keyholing is expected at this P-V combination, the sectioning was not perfectly perpendicular to the melt pool due to the 67 degree rotation of the beam the keyholing is not as obvious.

Powder Simulations:

A representative image of the results of the single beads with 20 μm of powder model can be seen in Figure 16, the gray area is the melted area, the purple shading shows where the powder layer is initially. From single bead simulation results we would expect a fairly semicircular melt pool. It can be easily seen that there is a slight deviation at the beginning of the powder layer but this is very slight. Comparatively, the simulation of an 80 μm powder layer (Figure 17) shows a much larger deviation from the nominal melt pool geometry.

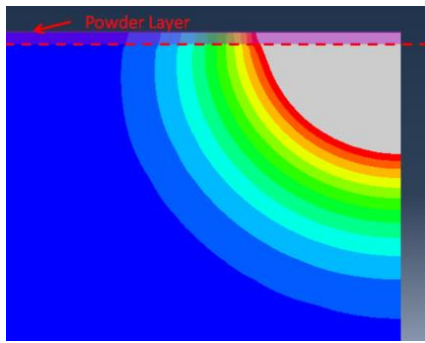


Figure 16: Melt pool cross section in powder simulation for 20 μm of added powder

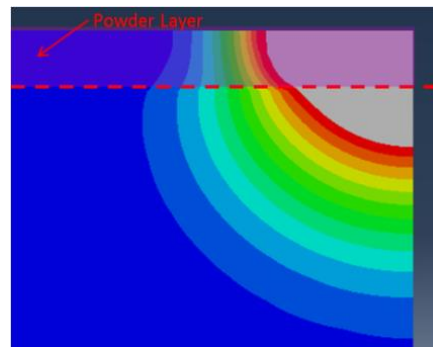


Figure 17: Melt pool cross section in powder simulation for 80 μm of added powder

Initial powder simulation results can be seen in Figure 18 and appear to show that powder layer thicknesses up to half of the no powder melt pool depth still yield results within 5% of the initial cross sectional area predicted by the no powder simulations for the same power and velocity combination. The same plot but with the x-axis presented in terms of the absolute depth of the powder layer is shown in Figure 19 for the nominal P-V case. The largest commonly used EOS layer thickness is 60 μm, and the predicted change in melt pool cross sectional area is still within 10% of the nominal cross sectional area. The lack of an effect of added powder in the cross sectional analysis of single bead experiments agrees with these predictions. Future work will investigate this trend throughout P-V space to see if this is valid for all P-V combinations.

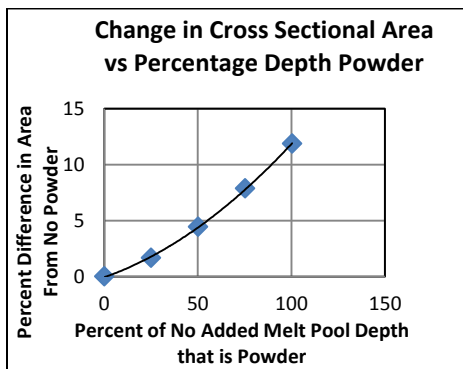


Figure 18: Change cross sectional area vs percentage depth powder

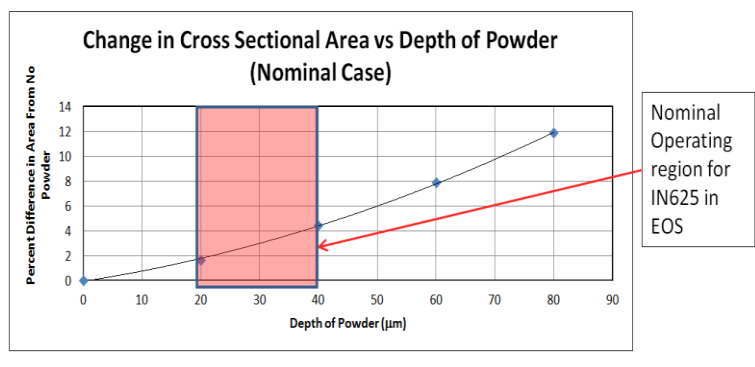


Figure 19: Change in cross sectional area vs depth of powder for nominal IN625 parameters

Conclusions

Process mapping techniques have been applied to the EOS region of beam Power-Velocity space yielding nearly linear curves of constant melt pool width and cross sectional area. The average absorptivity calculated across all P-V combinations is similar to values found in the literature for comparable lasers on Inconel but it does seem to vary through P-V space with a dependence on cross sectional area. A 20 μm powder layer appears to have a negligible effect on results in both powder simulations and experiments, but from powder simulations it appears that a thicker layer could result in a more noticeable (yet still small) effect. From preliminary cross sectional analysis of multi-layer pads, grains appear to be growing through multiple layers of powder and single bead results translate well to pad geometries in terms of melt pool geometry.

Acknowledgements

The authors wish to acknowledge Shawn Moylan of the National Institute of Standards and Technology (NIST) for performing the experiments and helping with experimental setup. The authors also wish to acknowledge Ross Cunningham of the Carnegie Mellon Materials Science and Engineering Department for help with imaging many of the samples. This work was supported by NIST under award #70NANB12H263.

References

- [1] J. Gockel and J. Beuth, "Understanding Ti-6Al-4V microstructure control in additive manufacturing via process maps," in *SFF*, Austin, TX, 2013.
- [2] F. Arcella and F. Froes, "Producing Titanium Aerospace Components from Powder Using Laser Forming," *JOM*, vol. 52, pp. 28-30, 2000.
- [3] J. Beuth and N. Klingbeil, "The Role of Process Variables in Laser-Based Direct Metal Solid Freeform Fabrication," *JOM*, no. September, pp. 36-39, 2001.
- [4] J. Beuth, J. Fox, J. Gockel, C. Montgomery, R. Yang, H. Qiao, E. Soylemez, P. Reeseewatt, A. Anvari, S. Narra and N. Klingbeil, "Process Mapping for Qualification Across Multiple Direct Metal Additive Manufacturing Processes," in *Solid Freeform Fabrication Symposium 2013 Proceedings*, Austin, TX, 2013.
- [5] Special Metals Corporation, "Inconel Alloy 625 Datasheet," 2013.
- [6] A. M. Anam, D. Pal and B. Stucker, "Modeling and experimental validation of nickel-based super alloy (Inconel 625) made using selective laser melting," in *SFF*, Austin, TX, 2013.
- [7] Kennametal, "High Temperature Machining Guide," [Online]. Available: http://www.kennametal.com/content/dam/kennametal/kennametal/common/Resources/Catalogs-Literature/Industry%20Solutions/SuperAlloys_material_machining_guide_Aerospace.pdf. [Accessed 2013].

- [8] E. Santos, F. Abe, Y. Kitamura, K. Osakada and M. Shiomi, "Mechanical properties of pure titanium models processed by selective laser melting," in *SFF*, Austin, TX, 2002.
- [9] A. Gratton, S. Kumpaty, S. Kamara, G. Raju, N. Panda, N. Kanoongo and K. Balasubramanian, "Comparison of mechanical, metallurgical properties of 17-4ph stainless steel between direct metal laser sintering (DMLS) and traditional manufacturing methods," in *National Conference On Undergraduate Research*, Ogden, Utah, 2012.
- [10] S. Bontha, "The Effect of Process Variables on Microstructure in Laser-Deposited Materials," 2006.
- [11] E. Soylemez, J. L. Beuth and K. Taminger, "Controlling Melt Pool Dimensions Over a Wide Range of Material Deposition Rates in Electron Beam Additive Manufacturing," in *Solid Freeform Fabrication Proceedings*, Austin, TX, 2010.
- [12] J. Fox and J. Beuth, "Process mapping of transient melt pool response in wire feed e-beam additive manufacturing of Ti-6Al-4V," in *SFF*, Austin, TX, 2013.
- [13] C. Sainte-Catherine, M. Jeandin, D. Kechemair and J.-P. Ricaud, "Study of Dynamic Absorptivity at 10.6 μ m (CO₂) and 1.06 μ m (Nd-YAG) Wavelengths as a Function of Temperature," *Journal De Physique IV*, vol. 1, no. C7, pp. 151-157, 1991.
- [14] R. Paschotta, "YAG Lasers," RP Photonics Consulting GmbH, Bad Dürkheim, 2012.
- [15] J. R. Howell, R. Siegel and M. P. Mengüç, *Thermal Radiation Heat Transfer*, 5th Edition ed., Boca Raton, FL: CRC Press, 2011.